**Supplementary Materials for**

# High-resolution structures of human PLPP3 reveal lipid binding and active-site organization

Yunhai Li[1, 2, 3, #], Cheng-Cen Guo[4, #], James Jiqi Wang[5, #], Qingning Yuan[1], Jiuyin Xu[1], Zhenyu Cao[6], Xiaoqi Guo[7], Wen Hu[3], Yichao Lin[3], Heng Zhang[3], Yong Li[2, *], H. Eric Xu[1, 3, 6, *] and Canrong Wu[1, *]

[#] These authors contributed equally

[*] Correspondence should be addressed to: Yong Li (yongli@xmu.edu.cn), H. Eric Xu (eric.xu@simm.ac.cn), or Canrong Wu (wcr13215@rjh.com.cn)

**This supplementary file includes:**

Materials and Methods

Supplementary Discussion

Supplementary Figures: S1 to S6

Supplementary Table S1

References

**Materials and Methods:**

**Cloning, protein expression, and purification**

The DNA sequence encoding full-length human PLPP3 (UniProt O14495-1) was cloned into the pEG BacMam expression vector containing an N-terminal FLAG tag and a C-terminal His tag. The construct was expressed in suspension HEK293E cells cultured in serum-free medium at 37°C with 5% $CO_2$. Cells at approximately 2.0 × 10^6 cells mL−1 were transfected using polyethylenimine at a DNA:polyethylenimine mass ratio of 1:3. Sodium butyrate (10 mM) was added 12-16 h after transfection, and cells were harvested 60 h after transfection. Cells were resuspended in 50 mM HEPES (pH 7.5), 150 mM NaCl, 10 µg mL−1 aprotinin, 4 µg mL−1 leupeptin, and 3 µg mL−1 pepstatin A, and disrupted on ice using a Dounce homogenizer.

Membranes were collected at 100,000 × g for 30 min at 4°C and solubilized for 2 h at 4°C in the same buffer containing 1% (w/v) dodecyl-β-D-maltoside and 0.2% (w/v) CHS. Insoluble material was removed at 100,000 × g for 40 min at 4°C. The supernatant was incubated with anti-FLAG M2 affinity resin for 2 h at 4°C. The resin was washed with buffer containing 0.03% (w/v) lauryl maltose neopentyl glycol (LMNG), 0.006% (w/v) CHS, and 0.01% (w/v) glyco-diosgenin (GDN), and bound protein was eluted with 0.4 mg mL−1 FLAG peptide. PLPP3 was further purified on a Superose 6 Increase 10/300 GL column equilibrated in 25 mM HEPES (pH 7.5), 150 mM NaCl, 0.0075% (w/v) LMNG, 0.0015% (w/v) CHS, and 0.0025% (w/v) GDN. Tetrameric peak fractions were pooled and concentrated to approximately 2.0 mg mL−1. For the preparation without added CHS, CHS was omitted from solubilization, affinity-purification, and size-exclusion buffers; GDN was retained at 0.01% (w/v) during affinity purification and 0.0025% (w/v) during size-exclusion chromatography. Labels reading “CHS-free” in figures denote the absence of added CHS, not the absence of other detergents. Mutant proteins were expressed and purified using the corresponding wild-type protocol.

**Cryo-EM sample preparation and data acquisition**

Purified CHS-bound apo, CHS-containing LPA-incubated, and without-added-CHS apo PLPP3 were concentrated to approximately 2 mg mL−1. For the product-state preparation, PLPP3 was incubated with LPA before grid preparation. Aliquots (3 μL) were applied to glow-discharged Quantifoil R1.2/1.3 Au 300-mesh grids, blotted for 3-4 s with a blot force of 2, and plunge-frozen in liquid ethane using a Vitrobot Mark IV. Data were collected on a Titan Krios G4 microscope operated at 300 kV and equipped with a K3 direct electron detector in counting mode. Movies were recorded at a nominal magnification of 165,000×, corresponding to a calibrated pixel size of 0.73 Å, with a total exposure of approximately 50 e− Å−2 and a defocus range of −1.0 to −3.0 μm.

**Cryo-EM data processing**

All datasets were processed in cryoSPARC using standard single-particle procedures (1). Movies were subjected to motion correction and contrast transfer function estimation. Particles were identified using complementary blob- and template-based picking; selected particles were used to train a Topaz particle picker (2). Redundant and duplicated particles were removed, and the final particle sets used for refinement and FSC estimation contained no duplicates. Extracted particles underwent iterative two-dimensional classification, ab initio reconstruction, and heterogeneous refinement. Subsequent three-dimensional refinement used non-uniform refinement (3). For the CHS-bound apo dataset, 7,382 movies yielded 1,476,215 initial particle projections, of which 401,323 contributed to the final reconstruction. For the CHS-containing LPA-incubated dataset, 8,000 movies yielded 1,311,261 initial projections. A subset of 548,410 particles was analyzed by three-dimensional variability analysis and display, followed by heterogeneous reconstruction; 195,060 particles contributed to the final map (4). For the

without-added-CHS apo dataset, 8,454 movies yielded 1,532,323 initial projections, of which 463,963 were retained. Each dataset was first refined without imposed symmetry (C1) using non-uniform and local refinement. C4 symmetry was then applied in subsequent refinement steps. Global resolutions were estimated from gold-standard Fourier shell correlation curves using the 0.143 criterion, and local-resolution maps were calculated in cryoSPARC.

**Model building, ligand assignment, and refinement**

An initial full-length human PLPP3 model was generated using AlphaFold 3 (5) and fitted into the CHS-bound apo map in UCSF ChimeraX (6). The model was rebuilt iteratively in Coot (7), and the refined CHS-bound apo model was used as the starting template for the LPA-incubated and without-added-CHS structures, which were rebuilt independently. Ligand coordinates and restraints were generated using eLBOW in PHENIX (8). CHS, cholesterol-like, phosphatidic acid-like, diacylglycerol-like, monoacylglycerol, and inorganic phosphate molecules were modeled only where density was continuous and compatible with ligand geometry and the local chemical environment. Densities with uncertain chemical identity were designated lipid-, sterol/acyl-, or acylglycerol-like. At the lateral site in the preparation without added CHS, trial fitting of GDN showed poorer agreement with the density and local pocket environment than cholesterol, and the cholesterol model was retained. Ordered waters were placed into discrete approximately spherical density peaks supported by plausible hydrogen-bonding geometry and retained only after refinement and map inspection. Models were refined in real space using PHENIX version 1.20.1-4487 with secondary-structure, stereochemical, and non-crystallographic-symmetry restraints as appropriate (8). Final models were evaluated using map-model correlation, Fourier shell correlation, and MolProbity validation (9).

**Site-directed mutagenesis and phosphatase activity assays**

K148A, R155A, E190A, S197A, H199A, R245A, H251A, R153A, H252A, P253A, F195A, Y75A, L52A, F45L, and Y106A substitutions were introduced by PCR-based site-directed mutagenesis and confirmed by Sanger sequencing. PLPP3 phosphatase activity was assessed by measuring inorganic phosphate release using a Malachite Green Phosphate Detection Kit (Beyotime Biotechnology, S0196M), with minor modifications to the manufacturer's protocol (10). For routine LPA assays, LPA sodium salt was dissolved directly in assay buffer containing 25 mM HEPES (pH 7.5), 150 mM NaCl, 0.0075% (w/v) LMNG, 0.0015% (w/v) CHS, and 0.0025% (w/v) GDN. Reactions were initiated by adding purified PLPP3 to a final enzyme concentration of 50 nM, with 200 μM LPA in a total volume of 150 μL.

Reactions were incubated at 37 °C for 10 min and stopped by adding 52.5 μL of phosphate-detection reagent. The mixtures were incubated at room temperature for 30 min, protected from light. A 60-μL aliquot was transferred to a 96-well plate, and absorbance was measured at 630 nm. Mutant activities were measured using identical enzyme and substrate concentrations within each experiment and normalized to WT PLPP3 analyzed in parallel. Time-course measurements supported the selected 10-min endpoint at the assay enzyme concentration, and a phosphate standard curve verified the linear detection range. Relative activities are reported relative to the corresponding WT or no-added-CHS reference, set to 100%.

For CHS-comparison experiments, WT PLPP3 was purified without added CHS throughout preparation. The baseline assay buffer contained 25 mM HEPES (pH 7.5), 150 mM NaCl, 0.0075% (w/v) LMNG, and 0.0025% (w/v) GDN, without added CHS. LPA for these comparisons was dissolved in this buffer without added CHS. CHS was dissolved in an LMNG-containing solution and added to a final concentration of 200 μM; the control received an

equal volume of the same LMNG solution without CHS. Enzyme, substrate, and vehicle additions were matched between comparison groups. PA-dependent phosphate release was also compared in the absence of added CHS and after addition of 200 μM CHS, with activity normalized to the corresponding control.

Absolute WT specific activities were 1705 ± 177 for LPA and 1314 ± 44 for PA without added CHS, and 2419 ± 299 for LPA and 1773 ± 58 for PA with 200 μM CHS (nmol Pi $min^{-1}$ $mg^{-1}$ protein; mean ± SD, n = 3). These correspond to increases of 41.9% and 34.9%, respectively. Specific activity is the amount of phosphate released (nmol), determined from the phosphate standard curve, divided by reaction time (min) and protein mass (mg).

**Statistical analysis**

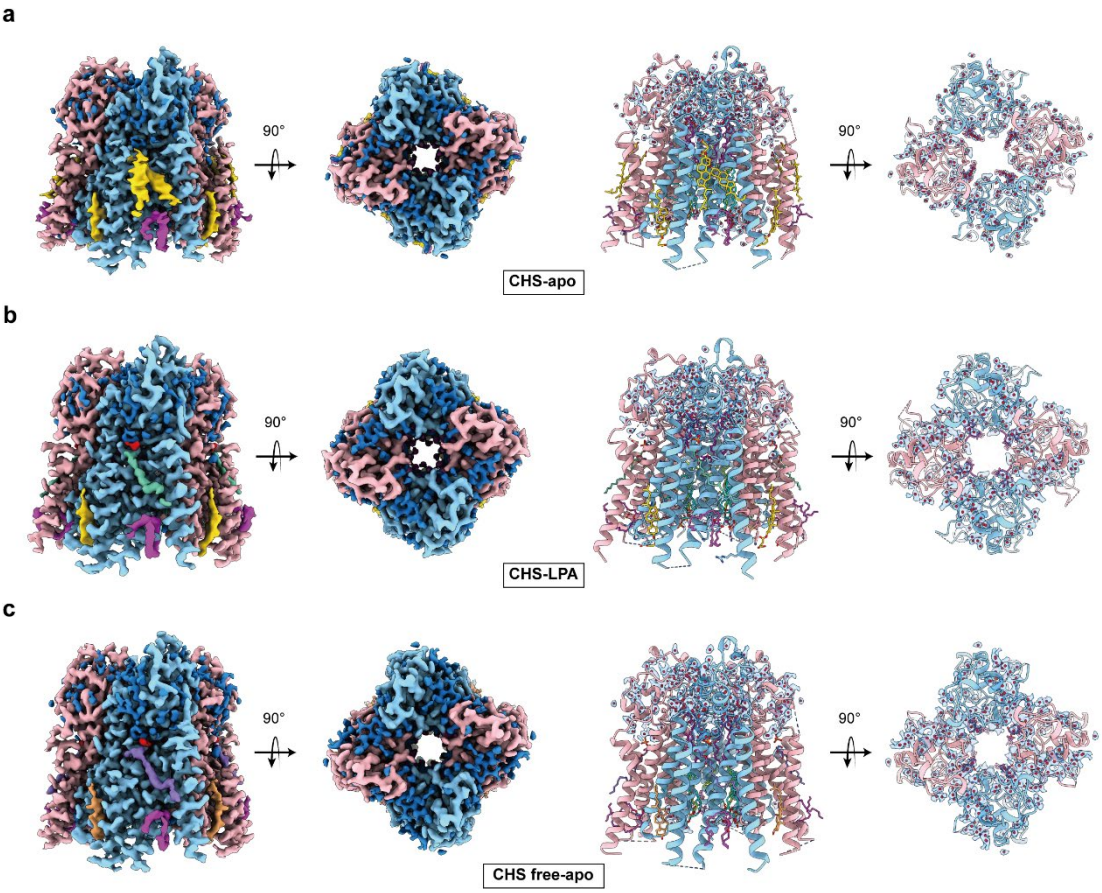
Statistical analyses were performed using GraphPad Prism 9.5. Relative activity plots are presented as means ± SEM; absolute WT specific activities are reported as means ± SD. Mutants were compared with wild-type PLPP3 by one-way analysis of variance followed by Dunnett's multiple-comparisons test (n = 3 independent measurements). Samples without added CHS and CHS-supplemented samples in the LPA comparison were compared using an unpaired two-tailed Student's t test (n = 3 independent measurements). $P < 0.05$ was considered statistically significant.

## Supplementary Discussion

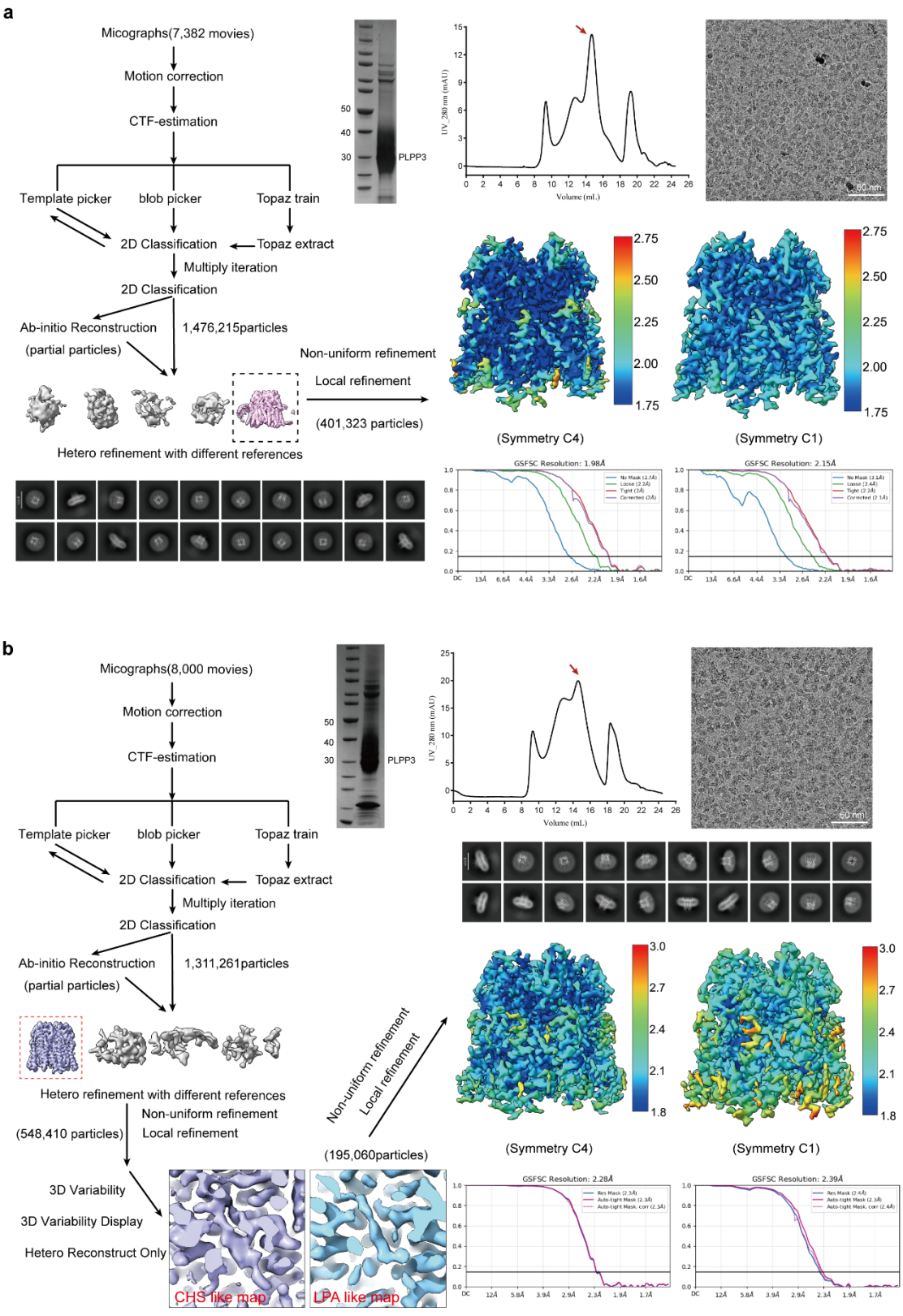
Interfacial substrate accommodation is an established feature of lipid-processing enzymes, including UGCG, which engages soluble and membrane-embedded substrates at a bipartite active site (11). The contribution of the present PLPP3 structures lies in the resolved lipid-binding geometries, ordered water network and active-site organization, rather than a new principle of interfacial catalysis.

CHS reproducibly enhanced activity toward both LPA and PA, but the measured response does not identify a particular binding site or establish allostery. CHS-1 and CHS-2 are resolved in the CHS-containing apo structure but not in the LPA-incubated product-compatible structure, whereas lateral CHS-3 remains bound (Supplementary Fig. S4). This pattern could reflect exchangeable access-region occupancy and a distinct lateral interaction that favors local packing, allowing net enhancement despite transient restriction of substrate access. However, the lateral CLR density without added CHS cautions against a simple empty-site filling model, and the existing mutant assays do not directly test CHS responsiveness. In mixed detergent–lipid systems, bulk solubilization does not fix substrate presentation at the interface; surface dilution kinetics provides a framework for evaluating these contributions (12). Matched LMNG controls do not exclude CHS-induced changes in micellar composition, substrate partitioning or protein stability during the assay.

Native cholesterol and cholesteryl esters have not been tested. Establishing sterol specificity and the mechanism of enhancement requires further work using validated sterol delivery and appropriate functional comparisons. Reconstitution in defined bilayers would provide a complementary test, although the low expression yield of PLPP3 currently limits such studies.



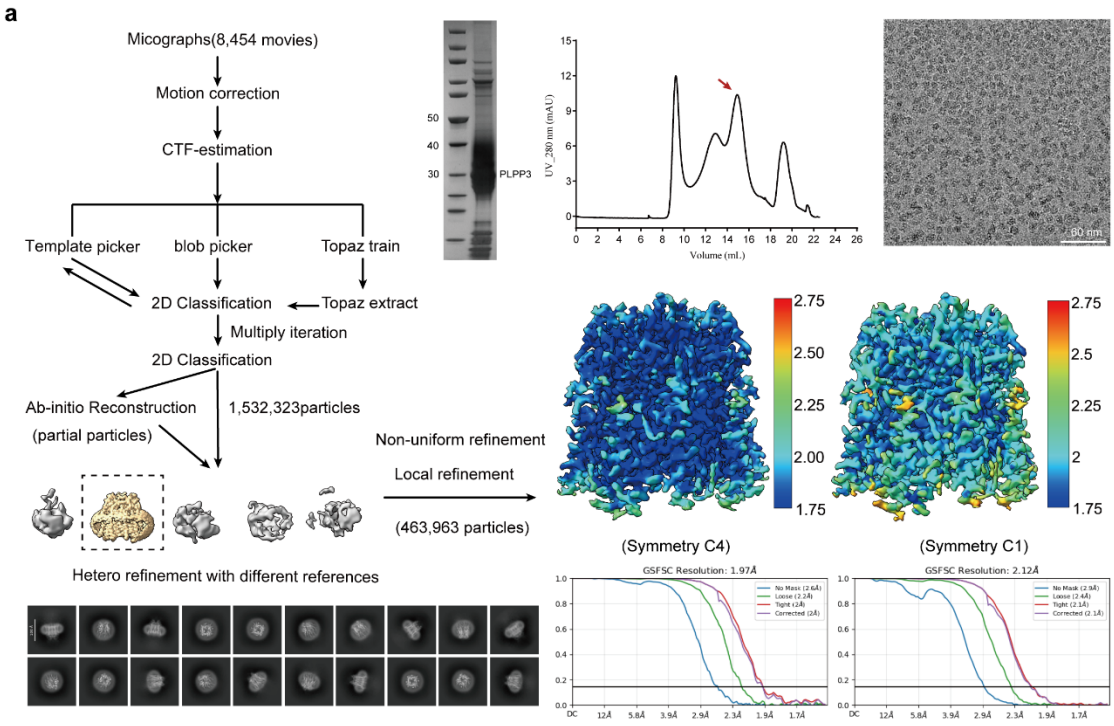

**Supplementary Fig. S1. Near-atomic cryo-EM structures reveal a conserved PLPP3 tetramer with extensive ordered hydration. a–c,** Cryo-EM density maps and corresponding atomic models of CHS-bound apo PLPP3 (**a**), CHS-containing LPA-incubated PLPP3 (**b**), and without-added-CHS apo PLPP3 (**c**), shown parallel to the membrane and after a 90° rotation about the tetramer axis. Alternating protomers are colored blue and salmon, and ordered lipid- and sterol-associated densities are shown in distinct colors. In the atomic models, ordered water molecules are shown as red spheres. All three structures adopt a closely conserved C4-symmetric tetrameric architecture and display extensive ordered hydration within the extracellular/luminal region, internal cavities, and membrane-proximal regions.



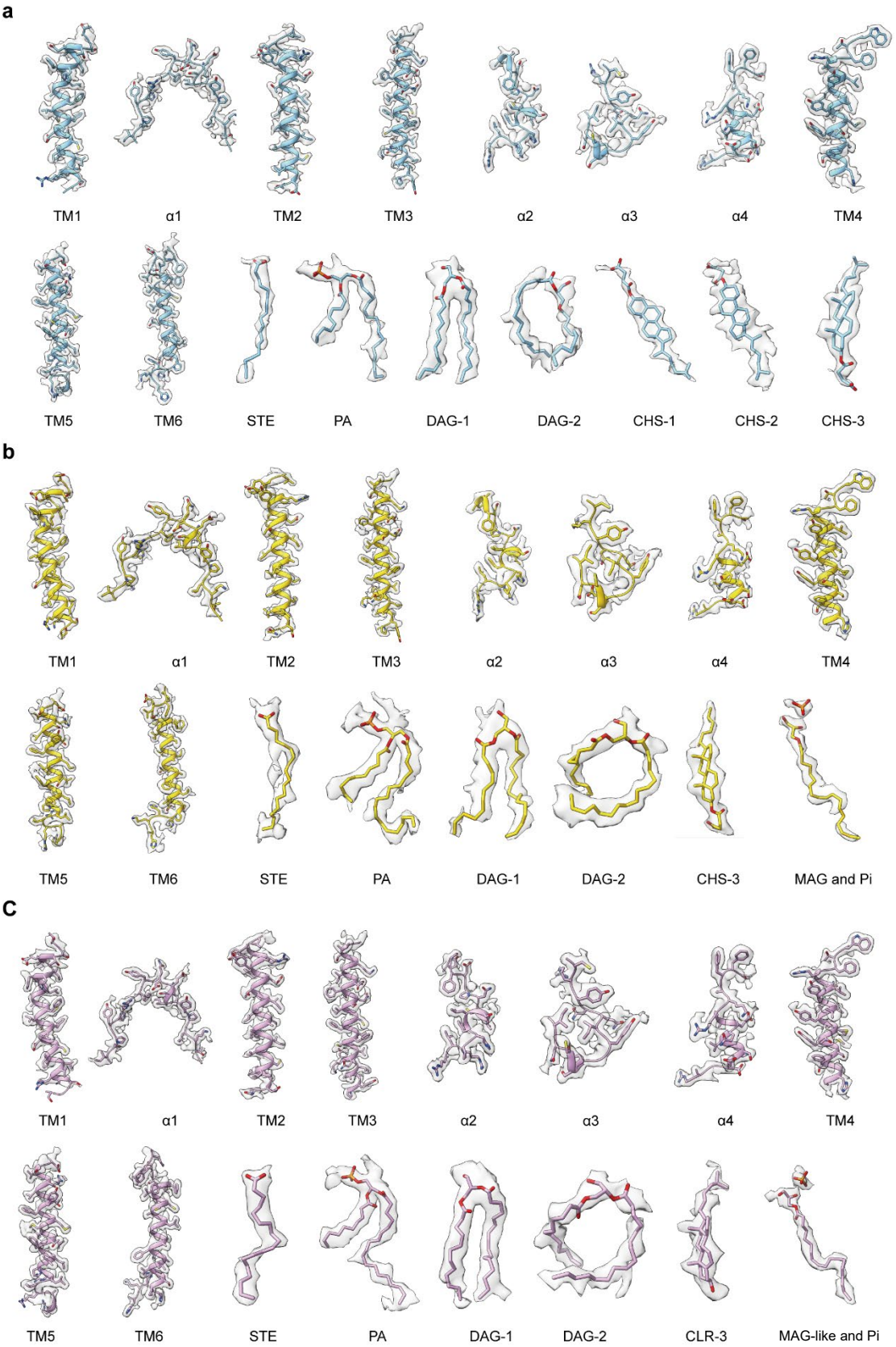

**Supplementary Fig. S2. Cryo-EM data processing and validation of CHS-bound apo and LPA-incubated PLPP3. a,** Purification, cryo-EM data-processing workflow, and reconstruction validation for CHS-bound apo PLPP3. The panel shows SDS-PAGE analysis, size-exclusion

chromatography, a representative micrograph, selected two-dimensional class averages, particle-selection and heterogeneous-refinement procedures, and local-resolution maps of the final C4- and C1-refined reconstructions. A total of 1,476,215 initially selected particles were subjected to iterative classification and heterogeneous refinement, yielding 401,323 particles for the final reconstruction. Gold-standard Fourier shell correlation (GSFSC) analysis yielded overall resolutions of 1.98 Å for the C4 reconstruction and 2.15 Å for the C1 reconstruction.

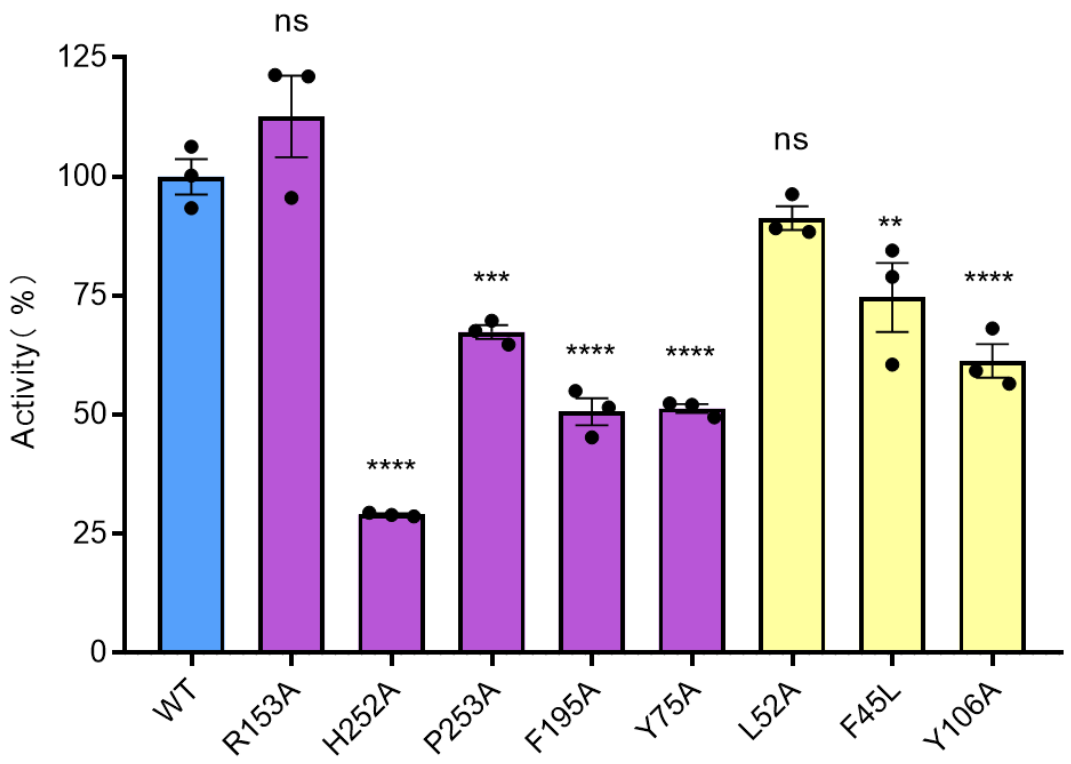
**b,** Purification, cryo-EM data processing, and validation of the CHS-containing LPA-incubated PLPP3 dataset. A total of 1,311,261 initially selected particles were subjected to iterative two-dimensional classification and heterogeneous refinement. A subset of 548,410 particles was further analyzed by three-dimensional variability analysis and display, followed by heterogeneous reconstruction to separate particles with CHS-like and LPA/product-associated densities. Subsequent non-uniform and local refinements yielded a final subset of 195,060 particles. Local-resolution maps and GSFSC curves show overall resolutions of 2.28 Å and 2.39 Å for the C4- and C1-refined reconstructions, respectively. Red arrows in the size-exclusion chromatography profiles indicate the fractions used for cryo-EM analysis.



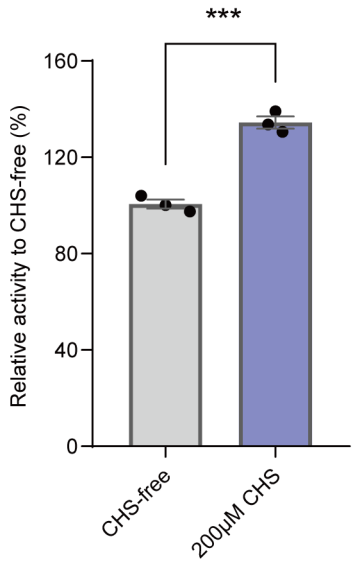

**Supplementary Fig. S3. Cryo-EM data processing and validation of without-added-CHS apo PLPP3. a,** Purification, cryo-EM data-processing workflow, and reconstruction validation for without-added-CHS apo PLPP3. The panel includes SDS-PAGE analysis, size-exclusion chromatography, a representative micrograph, selected two-dimensional class averages, ab initio reconstruction, heterogeneous refinement, and local-resolution maps of the final C4- and C1-refined reconstructions. A total of 1,532,323 initially selected particles were subjected to iterative classification and heterogeneous refinement, yielding 463,963 particles for the final reconstruction. Gold-standard Fourier shell correlation (GSFSC) analysis yielded overall resolutions of 1.97 Å for the C4 reconstruction and 2.12 Å for the C1 reconstruction. The red arrow in the size-exclusion chromatography profile indicates the fraction used for cryo-EM analysis.


a
TM1
α1
TM2
TM3
α2
α3
α4
TM4
TM5
TM6
STE
PA
DAG-1
DAG-2
CHS-1
CHS-2
CHS-3
b
TM1
α1
TM2
TM3
α2
α3
α4
TM4
TM5
TM6
STE
PA
DAG-1
DAG-2
CHS-3
MAG and Pi
C
TM1
α1
TM2
TM3
α2
α3
α4
TM4
TM5
TM6
STE
PA
DAG-1
DAG-2
CLR-3
MAG-like and Pi

**Supplementary Fig. S4. Representative local cryo-EM densities support high-confidence modeling of PLPP3 and associated membrane lipids. a–c,** Representative local cryo-EM densities from the CHS-bound apo (**a**), CHS-containing LPA-incubated product state (**b**), and without-added-CHS apo (**c**) PLPP3 structures. For each state, densities are shown for transmembrane helices TM1–TM6, extracellular/luminal helices α1–α4, and selected non-protein ligands. Shared membrane-associated densities include a sterol/acyl-like density (STE), a phosphatidic acid-like density (PA), and two diacylglycerol-like densities (DAG-1 and DAG-2). The CHS-bound apo structure additionally resolves three cholesterol hemisuccinate molecules, CHS-1, CHS-2, and CHS-3. The LPA-incubated product state resolves CHS-3 together with monoacylglycerol (MAG) and inorganic phosphate (Pi). In the without-added-CHS apo structure, a cholesterol-like density (CLR) occupies the lateral site corresponding to CHS-3, whereas a MAG-like density and Pi are resolved in the membrane-access pocket and catalytic chamber, respectively. Gray surfaces represent the corresponding cryo-EM densities. The close agreement between the fitted models and local densities supports high-confidence modeling of the PLPP3 protein scaffold and the assigned lipid- and product-associated ligands.




**Supplementary Fig. S5. Effects of PLPP3 substitutions on LPA phosphatase activity.** Activities of WT PLPP3 and the indicated mutants were measured by monitoring inorganic phosphate release using the malachite-green assay. Reactions contained 50 nM enzyme and 200 μM LPA and were incubated at 37 °C for 10 min. Activities were normalized to the mean WT activity (100%). Y75 and F195 participate in interprotomer contacts, whereas P253 lines an interfacial lipid-binding cleft. Each dot represents an independent experiment (n = 3 per group); bars show mean ± SEM. Statistical comparisons with WT were performed using one-way ANOVA followed by Dunnett's multiple comparisons test. ns, not significant; **P < 0.01; ***P < 0.001; ****P < 0.0001.




**Supplementary Fig. S6. Effect of CHS on PA hydrolysis by PLPP3.** PA-dependent phosphate release was measured using PLPP3 purified without added CHS, in the absence or presence of 200 μM CHS. The control received an equivalent volume of the LMNG vehicle. Activities were normalized to the mean activity of the control without added CHS (100%). Each dot represents an independent experiment (n = 3 per group); bars show mean ± SEM. ***P < 0.001.

**Supplementary Table S1**

Cryo-EM data collection, refinement, and validation statistics for the three PLPP3 structures.

| | CHS-apo | CHS-LPA | No-added-CHS apo |
|---|---|---|---|
| **Data collection and processing** | | | |
| Magnification | 165,000 | 165,000 | 165,000 |
| Voltage (kV) | 300 | 300 | 300 |
| Electron exposure ($e^{-}$/Å$^2$) | 50 | 50 | 50 |
| Defocus range (μm) | -1.0~-3.0 | -1.0~-3.0 | -1.0~-3.0 |
| Pixel size (Å) | 0.73 | 0.73 | 0.73 |
| Symmetry imposed | C4 | C4 | C4 |
| Initial particle projections (no.) | 1,476,215 | 1,311,261 | 1,532,323 |
| Final particle projections (no.) | 401,323 | 195,060 | 463,963 |
| Map resolution (Å) | 1.98 | 2.28 | 1.97 |
| Map resolution range (Å) | 1.75-2.75 | 1.80-3.00 | 1.75-2.75 |
| FSC threshold | 0.143 | 0.143 | 0.143 |
| **Model Refinement** | | | |
| Refinement package | PHENIX-1.20.1-4487 | PHENIX-1.20.1-4487 | PHENIX-1.20.1-4487 |
| Real or reciprocal space | Real space | Real space | Real space |
| Model-Map CC (mask) | 0.87 | 0.88 | 0.88 |
| Model resolution (Å) | 2.0 | 2.3 | 2.0 |
| FSC threshold | 0.5 | 0.5 | 0.5 |
| B factors (Å2, mean value) | | | |
| Protein residues | 30.86 | 26.13 | 41.29 |
| Ligands | 44.21 | 34.62 | 53.02 |
| Water | 36.36 | 24.24 | 44.75 |
| **Model composition** | | | |
| Non-hydrogen atoms | 8726 | 8512 | 8606 |
| Protein residues | 944 | 944 | 948 |
| R.m.s. deviations | | | |
| Bond lengths (Å) | 0.005 | 0.003 | 0.003 |
| Bond angles (°) | 0.694 | 0.577 | 0.572 |
| **Validation** | | | |
| MolProbity score | 1.33 | 1.34 | 1.07 |
| Clashscore | 6.03 | 6.13 | 2.83 |
| Rotamer outliers (%) | 0 | 0.98 | 0.49 |
| Ramachandran plot | | | |
| Favored (%) | 98.70 | 98.26 | 99.13 |
| Allowed (%) | 1.30 | 1.74 | 0.87 |
| Disallowed (%) | 0 | 0 | 0 |
| **Data availability** | | | |
| EMDB entry | EMD-85000 | EMD-84998 | EMD-84999 |
| PDB entry | 47ZH | 47ZF | 47ZG |

## References


1. Punjani, A., Rubinstein, J.L., Fleet, D.J. & Brubaker, M.A. Nat. Methods 14, 290–296 (2017).
2. Bepler, T. et al. Nat. Methods 16, 1153–1160 (2019).
3. Punjani, A., Zhang, H. & Fleet, D.J. Nat. Methods 17, 1214–1221 (2020).
4. Punjani, A. & Fleet, D.J. J. Struct. Biol. 213, 107702 (2021).
5. Abramson, J. et al. Nature 630, 493–500 (2024).
6. Pettersen, E.F. et al. Protein Sci. 30, 70–82 (2021).
7. Emsley, P., Lohkamp, B., Scott, W.G. & Cowtan, K. Acta Crystallogr. D Biol. Crystallogr. 66, 486–501 (2010).
8. Liebschner, D. et al. Acta Crystallogr. D Struct. Biol. 75, 861–877 (2019).
9. Williams, C.J. et al. Protein Sci. 27, 293–315 (2018).
10. Lanzetta, P.A., Alvarez, L.J., Reinach, P.S. & Candia, O.A. Anal. Biochem. 100, 95–97 (1979).
11. Wu, C. et al. Nature 657, 549–558 (2026).
12. Carman, G.M., Deems, R.A. & Dennis, E.A. J. Biol. Chem. 270, 18711–18714 (1995).